

Chapter 21

Integrated DEM Construction and Calibration of Hyperspectral Imagery: A Remote Sensing Perspective

Christian Wöhler and Arne Grumpe

Abstract In this study, we present from a remote sensing perspective a method for the combination of surface gradient information obtained by photoclinometry and shape from shading with absolute depth data (here: light detection and ranging (LIDAR) data) by exploiting their respective advantages, regarding distinctly non-Lambertian surfaces with non-uniform albedos. While photometry-based 3D reconstruction methods yield reliable small-scale surface gradient information for each image pixel, absolute depth data which are typically noisy on small scales but reliable on large scales are provided by LIDAR techniques. The first step of the proposed algorithm consists of an extended photoclinometry approach which takes into account both image and LIDAR data. In a second step the reconstructed surface is refined based on an iterative scheme relying on the minimisation of a global error functional, thus compensating the inaccuracies of the measured surface gradients and the LIDAR data on the respective scales. The surface shape and non-uniform albedo map represent the best fit to the observed image radiances and LIDAR data. We apply our framework to the construction of digital elevation models (DEM) of lunar surface regions. We use hyperspectral imagery in order to employ the DEM to normalise the wavelength-dependent surface reflectance to a standard illumination and viewing geometry. Although we employ a highly realistic, physically motivated reflectance model (the Hapke model), systematic topography-dependent distortions of the pixel spectra occur, which lead to errors in the extracted spectral parameters (e.g. the absorption wavelength, depth, and width of prominent absorption troughs) and for which we propose an empirical, PCA-based correction approach. Based on the correspondingly corrected surface reflectances we obtain a refined DEM along with spectral parameter maps in which (except for the hydroxyl absorption) topographic effects are nearly completely removed.

C. Wöhler (✉) · A. Grumpe

Image Analysis Group, Dortmund University of Technology, Otto-Hahn-Str. 4,
44227 Dortmund, Germany

e-mail: christian.woehler@tu-dortmund.de; arne.grumpe@tu-dortmund.de

21.1 Introduction

The concept of photoclinometry is introduced by Wilhelms [52] for the image-based measurement of lunar surface slopes. The concepts of shape from shading and photometric stereo are introduced by Horn [20] and Woodham [54], respectively. The method of characteristic strip expansion by Horn [21] and also the method by Kozera [29] directly yield a depth map of the surface. In contrast, other methods by Horn [20, 22] estimate the gradient field of the surface and infer the depth map by integration. The computational efficiency of such gradient-based approaches is increased e.g. by Simchony et al. [47] by an analytical approach. An extensive survey is provided in [1].

Improved results can be achieved by combining photometrically determined surface gradient data with independently measured absolute depth data. General solutions for this problem are proposed e.g. in [7] and [40], where a highly detailed 3D surface reconstruction is obtained by a combination of the low-frequency part of the absolute depth data with the high-frequency component of the photometrically determined surface gradients. Non-Lambertian metallic surfaces are reconstructed e.g. in [53], multiple views are taken into account in [25, 32, 55], and moving objects are analysed in [46].

In the context of lunar remote sensing, a global digital elevation model (DEM) of the Moon of 100 m nominal lateral resolution with a typical vertical accuracy of 23 m is described in [44], which is termed “GLD100” and has been constructed based on the stereoscopic evaluation of images acquired by the LROC WAC (Lunar Reconnaissance Orbiter Wide Angle Camera). LROC NAC (Narrow Angle Camera) based stereo images analysis has led to the construction of local lunar DEMs of very high lateral resolution [31, 36]. Detailed information about the LROC WAC and NAC instruments can be found in [43]. A nearly global lunar hyperspectral image mosaic of typically 140 m resolution has been acquired by the Moon Mineralogy Mapper (M^3) instrument on board the Indian spacecraft Chandrayaan-1 [42] (<http://m3.jpl.nasa.gov/m3data.html>).

A combination of stereo image analysis and shape from shading is used in [28] to construct DEMs of high lateral resolution of the surface of Mars. Lunar DEMs are generated in [33] based on images acquired by the Clementine spacecraft using a technique termed “multi-image shape from shading”, where the elevation values and the parameters of the surface reflectance function are adapted to the image radiance information, assuming a uniform surface albedo. A photometric stereo method is used for DEM construction in [10] based on overlapping images of the lunar southern polar region acquired by the SMART-1 Advanced Moon micro-Imager Experiment (AMIE) camera. Detailed information about the AMIE instrument can be found in [26]. The properties of the recently acquired lunar orbital image data sets are summarised in Table 21.1.

The global DEMs obtained by the LIDAR instrument LALT on board the Japanese Kaguya spacecraft and the Lunar Orbiter Laser Altimeter (LOLA) instrument on board the LRO spacecraft have vertical accuracies of a few metres (cf. [4] and [31] for a short description of LALT and LOLA data, respectively). The nominal

Table 21.1 Properties of recently acquired lunar orbital imagery. The numbers in brackets denote the M³ target mode applied to selected regions only

Instrument	Bands	Wavelength (nm)	Resolution (m/pixel)	Reference
SMART-1 AMIE	No filter + 3	Visible, 750–960	27–270	[26]
Chandrayaan-1 M ³	85 (260)	461–2,976	140 (70)	[42]
LROC WAC	7	320–690	100	[43]
LROC NAC	1	Visible	0.5	[43]

lateral resolution of the gridded LOLA DEM (available at <http://pds-geosciences.wustl.edu/missions/lro/lola.htm>) corresponds to 30 m at the lunar equator, but its effective lateral resolution is several times lower in most regions due to missing data and the resulting interpolation artifacts.

This study presents a method for the integration of surface gradient data obtained by shape from shading with absolute depth data inferred from laser altimetry measurements, relying on M³ orbital images and the global LOLA DEM. This framework is applied to the construction of DEMs of the lunar surface, which displays a non-Lambertian reflectance behaviour and a non-uniform albedo. The resulting DEMs have a high effective lateral resolution that comes close to the pixel resolution of the utilised images. Furthermore, based on the resulting DEM data we introduce the first procedure (to our knowledge) that normalises wavelength-dependent lunar surface reflectance values to a standard illumination and viewing geometry based on the topography on large and small spatial scales (given the corresponding values of the pixel resolution, large spatial scales will in the following refer to kilometres and small scales to pixels).

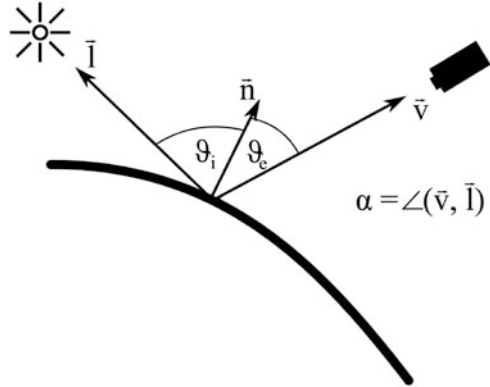
21.2 Reflectance Modelling

The light power emitted by a unit surface into a unit solid angle is termed “radiance” and is measured in $\text{W m}^{-2} \text{sr}^{-1}$. The incoming light power per apparent unit surface is termed “irradiance” and has the physical unit W m^{-2} . The so-called “reflectance” is defined as the ratio between radiance and irradiance [21]. It usually depends on the incidence angle θ_i between the surface normal \mathbf{n} and the direction \mathbf{l} to the light source, the emission angle θ_e between \mathbf{n} and the direction \mathbf{v} to the camera, and on the phase angle α between the vectors \mathbf{l} and \mathbf{v} [14] (Fig. 21.1). The radiances and irradiances regarded in the experiments of this study are additionally normalised to wavelength (“spectral radiance” and “spectral irradiance” [14, 27]).

A reflectance model based on the theory of radiative transfer [5] has been proposed by Hapke [14–17], which in its general form according to [17] can be written as

$$R_{\text{AMSA}}(\mu_0, \mu, \alpha) = \frac{w}{4\pi} \frac{\mu_0}{\mu_0 + \mu} [p(\alpha) B_{\text{SH}}(\alpha) + M(\mu_0, \mu)] B_{\text{CB}}(\alpha) \quad (21.1)$$

Fig. 21.1 Illustration of the illumination and observation geometry



with $\mu_0 = \cos \theta_i$ and $\mu = \cos \theta_e$. According to [14–17], the intrinsic reflectivity of a surface particle is denoted by w and is termed “single-scattering albedo”. Typical planetary surfaces display a peak of the reflectance function around $\alpha = 0^\circ$. This so-called “opposition effect” is composed of a shadow hiding [16, 17] and a coherent backscatter [17] component, described by the functions $B_{SH}(\alpha)$ and $B_{CB}(\alpha)$ in Eq. (21.1), respectively. Each of these functions is governed by two parameters describing the strength and width of the respective component [17]. The function $p(\alpha)$ is the so-called “single-particle scattering function” describing first-order scattering processes at the particles [14]. The term $M(\mu_0, \mu)$ according to [17] describes multiple scattering processes, which are assumed to be isotropic in [14–16], leading to the “isotropic multiple scattering approximation” (IMSA), while $p(\alpha)$ is expanded as a series of Legendre polynomials in [17], resulting in the “anisotropic multiple scattering approximation” (AMSA). An extension that takes into account the roughness of the surface is introduced in [15].

The so-called “lunar-Lambert” function, a simplified, empirical reflectance function for planetary surfaces, is proposed in [38] according to

$$R_{LL}(\mu_0, \mu, \alpha) = \rho \left[2L(\alpha) \frac{\mu_0}{\mu_0 + \mu} + (1 - L(\alpha)) \mu_0 \right]. \quad (21.2)$$

The factor ρ depends on the reflectivity of the surface but also on camera-specific factors such as the sensor sensitivity. The empirical function $L(\alpha)$ is determined in [38] based on a phase angle specific maximisation of the similarity between the lunar-Lambert reflectance $R_{LL}(\mu_0, \mu, \alpha)$ and the Hapke IMSA reflectance [14–16] across a broad interval of incidence and emission angles for a variety of parameter configurations of the Hapke IMSA model.

The lunar-Lambert model is commonly used as the basis for the normalisation of reflectance data to a standard illumination and viewing geometry, as outlined e.g. in [39]. It is favourably used for DEM construction if relative pixel intensities rather than absolute radiance data are available.

In the DEM construction framework proposed in Sect. 21.3, radiance images are evaluated, where the generally non-uniform value of the single-scattering albedo w is recovered for each surface location simultaneously with the DEM, while the other parameters of the Hapke model [14–17] are adopted from [51] (Moon solution 1 therein) and are assumed to be constant.

21.3 DEM Construction

In the following, the surface gradients are denoted by p and q , implying a local surface normal vector $\mathbf{n} = (-p, -q, 1)^T$, the surface by z , the observed radiance by L^{obs} , the solar irradiance by E^{sun} , the modelled reflectance by R , and the lateral coordinates by x and y . The value of E^{sun} depends on the wavelength range in which the image has been acquired and is assumed to be known. In our remote sensing scenario, the observed reflectance is computed by a pixel-wise division of L^{obs} by E^{sun} . For brevity, the dependence on x and y is omitted where possible.

21.3.1 The Error Functional

The description in this section and in Sect. 21.3.2 has been adapted from [18]. Horn [22] proposes a minimisation of a global error functional composed of the reflectance error

$$E_R = \iint \left(\frac{L^{\text{obs}}(x, y)}{E^{\text{sun}}} - R(p(x, y), q(x, y)) \right)^2 dx dy \quad (21.3)$$

and the integrability error

$$E_{\text{int}} = \iint \left[(z_x - p)^2 + (z_y - q)^2 \right] dx dy. \quad (21.4)$$

We extend this framework by adding the error term

$$\begin{aligned} E_{\text{DEM}} = & \iint \left[f_{\sigma_{\text{DEM}}} \left(\frac{\partial z_{\text{DEM}}}{\partial x} \right) - f_{\sigma_{\text{DEM}}}(p) \right]^2 \\ & + \left[f_{\sigma_{\text{DEM}}} \left(\frac{\partial z_{\text{DEM}}}{\partial y} \right) - f_{\sigma_{\text{DEM}}}(q) \right]^2 dx dy \end{aligned} \quad (21.5)$$

to the error functional $E = E_R + \gamma E_{\text{int}}$ proposed in [22], such that absolute depth data z_{DEM} like the LOLA DEM can be taken into account. The term E_{DEM} takes into account the deviation between the large-scale gradients of the depth data and

the surface z . The noisy high-frequency component of the absolute depth data is suppressed by the lowpass filter function $f_{\sigma_{\text{DEM}}}$, which is implemented as a Gaussian filter of width σ_{DEM} . The low-frequency component of the absolute depth data can be expected to be accurate on large scales. The reconstruction error E_{Σ} to be minimised thus corresponds to

$$E_{\Sigma} = E_R + \gamma E_{\text{int}} + \delta E_{\text{DEM}} \quad (21.6)$$

with γ and δ as weight parameters.

At this point one might argue that it would be more straightforward to take into account the low-frequency component of z_{DEM} directly instead of the corresponding surface gradients. However, a computationally efficient formulation comparable to the gradient-based numerical scheme presented in Sect. 21.3.2 is not available, such that an error term based on z_{DEM} would be much more intricate to minimise. Furthermore, the normalisation of the hyperspectral data described in Sect. 21.5 requires accurate values of the surface gradients rather than the surface itself, such that we expect an explicit determination of the surface gradients to be beneficial in that context.

21.3.2 Variational Optimisation Scheme

The minimisation of E_{Σ} with a nonzero value of γ aims for generating an integrable surface gradient field. For this purpose, we use a variational scheme according to [22], leading to

$$\begin{aligned} p^{(n+1)} &= z_x^{(n)} + \frac{1}{\gamma} \left[\frac{L^{\text{obs}}}{E^{\text{sun}}} - R(z_x^{(n)}, z_y^{(n)}) \right] \frac{\partial R}{\partial p} \bigg|_{z_x^{(n)}} \\ &\quad + \frac{\delta}{\gamma} \iint \left[f_{\sigma_{\text{DEM}}} \left(\frac{\partial z_{\text{DEM}}}{\partial x} \right) - f_{\sigma_{\text{DEM}}}(z_x^{(n)}) \right] \frac{\partial f_{\sigma_{\text{DEM}}}(p)}{\partial p} \bigg|_{z_x^{(n)}} dx dy \\ z^{(n+1)} &= \bar{z}^{(n)} - \frac{\varepsilon^2}{\kappa} \left[p_x^{(n+1)} + q_y^{(n+1)} \right]. \end{aligned} \quad (21.7)$$

The corresponding equation for q is obtained analogously. In Eq. (21.7), the average over the κ nearest neighbouring pixels is denoted by \bar{z} , and the lateral offset between neighbouring pixels is given by ε . The surface may be initialised e.g. by the LOLA DEM.

The double integral in Eq. (21.7) corresponds to $\frac{\partial E_{\text{DEM}}(p, q)}{\partial p}$. A computationally efficient implementation is obtained for the complete image by two consecutive linear filtering operations if the filtering function $f_{\sigma_{\text{DEM}}}$ is implemented as a linear filter. According to [13], the double integral is written as a sum over $U \times V$ discrete cells, where the filter function $f_{\sigma_{\text{DEM}}}$ is defined as a $K \times L$ filter matrix $F_{\sigma_{\text{DEM}}}$, leading to

$$\begin{aligned} \frac{\partial E_{\text{DEM}}(p, q)}{\partial p} = & - \sum_{i=1}^U \sum_{j=1}^V A(i, j) \left[\sum_{k=-K/2}^{K/2} \sum_{l=-L/2}^{L/2} F_{\sigma_{\text{DEM}}}(k, l) \left(\frac{\partial z_{\text{DEM}}}{\partial x} \right) \Big|_{i+k, j+l} \right. \\ & \left. - p(i+k, j+l) \right] \left[\sum_{k=-K/2}^{K/2} \sum_{l=-L/2}^{L/2} F_{\sigma_{\text{DEM}}}(k, l) \frac{\partial p(i+k, j+l)}{\partial p} \Big|_{u, v} \right]. \quad (21.8) \end{aligned}$$

In Eq. (21.8), the filter $f_{\sigma_{\text{DEM}}}$ is correlated with the discrete data. The areal extent $A(i, j)$ of a discrete cell is defined such that it denotes the surface area covered by the respective pixel. This quantity is not necessarily identical for all pixels. The summands in Eq. (21.8) are only non-zero for $u = l + k$ and $v = j + l$. Omitting the zero-valued summands and shifting the indices i and j such that they are centred at u and v yields

$$\begin{aligned} \frac{\partial E_{\text{DEM}}(p, q)}{\partial p} = & - \sum_{i=-K/2}^{K/2} \sum_{j=-L/2}^{L/2} F_{\sigma_{\text{DEM}}}(-i, -j) \left[\sum_{k=-K/2}^{K/2} \sum_{l=-L/2}^{L/2} F_{\sigma_{\text{DEM}}}(k, l) \right. \\ & \left. \times \left(\frac{\partial z_{\text{DEM}}}{\partial x} \Big|_{u+k+i, v+l+j} - p(u+k+i, v+l+j) \right) \right] A(u+i, v+j) \quad (21.9) \end{aligned}$$

$$\begin{aligned} \frac{\partial E_{\text{DEM}}(p, q)}{\partial q} = & - \sum_{i=-K/2}^{K/2} \sum_{j=-L/2}^{L/2} F_{\sigma_{\text{DEM}}}(-i, -j) \left[\sum_{k=-K/2}^{K/2} \sum_{l=-L/2}^{L/2} F_{\sigma_{\text{DEM}}}(k, l) \right. \\ & \left. \times \left(\frac{\partial z_{\text{DEM}}}{\partial y} \Big|_{u+k+i, v+l+j} - q(u+k+i, v+l+j) \right) \right] A(u+i, v+j). \quad (21.10) \end{aligned}$$

According to Eq. (21.9), $\frac{\partial E_{\text{DEM}}(p, q)}{\partial p}$ is obtained by a correlation between the filter matrix $F_{\sigma_{\text{DEM}}}$ and the difference between the surface gradient $\frac{\partial z_{\text{DEM}}}{\partial x}$ of the absolute depth map and the surface gradient p to be optimised, and in a second step a convolution of the correlation result with the filter matrix $F_{\sigma_{\text{DEM}}}$ weighted by the areal extent $A(i, j)$. The value of $\frac{\partial E_{\text{DEM}}(p, q)}{\partial q}$ is obtained in an analogous manner (cf. Eq. (21.10)). The order of correlation and convolution in Eqs. (21.9) and (21.10) is exchanged if the filter function $f_{\sigma_{\text{DEM}}}$ is defined by a convolution rather than a correlation.

For a simultaneous reconstruction of the surface and the spatially non-uniform albedo, the optimisation according to Eq. (21.7) is incorporated into a further iterative scheme. The angles $\theta_i^{(m)}$ and $\theta_e^{(m)}$ and their cosines $\mu_0^{(m)}$ and $\mu^{(m)}$ are determined based on the surface $z^{(m)}$ and the corresponding gradients $p^{(m)}$ and $q^{(m)}$ for each iteration m . The non-uniform single-scattering albedo $w^{(m)}(x, y)$ is obtained by solving

$$R\left(\mu_0^{(m)}, \mu^{(m)}, \alpha, w^{(m)}(x, y)\right) = \frac{L^{\text{obs}}(x, y)}{E_{\text{sun}}} \quad (21.11)$$

with respect to $w^{(m)}(x, y)$ for each pixel (x, y) . A Gaussian low-pass filter $G_{\sigma_w^{(m)}}$ of width $\sigma_w^{(m)}$ is then convolved with $w^{(m)}(x, y)$. The surface gradients $p(m+1)$, $q(m+1)$, and the surface $z(m+1)$ of the subsequent step $(m+1)$ are computed based on the filtered albedo map $\left[G_{\sigma_w^{(m)}} * w^{(m)}(x, y) \right]$. The width parameter $\sigma_w^{(m)}$ is decreased in the course of the iteration process such that an albedo map of increasing spatial resolution is obtained.

21.3.3 Initialisation by an Extended Photoclinometry Scheme

Photoclinometry denotes the pixel-wise determination of the surface gradients according to the observed image reflectances by setting the reflectance error E_R (cf. Eq. (21.3)) to zero for each pixel [22]. However, if only a single image is available but two surface gradients and (in the case of a non-uniform albedo map) the surface albedo need to be estimated, this ill-posed problem has an infinite number of solutions. Commonly, assumptions are made that regularise the problem and reduce the solution space to a single solution. For example, the albedo might be assumed to be constant over the surface or line-wise constant in the azimuthal direction of incident light. Additionally, the gradient perpendicular to the azimuthal direction of the incident light is difficult to estimate accurately; if it is small, it may be set to zero [22]. A constant or line-wise constant albedo can be estimated when the mean surface slope on large spatial scales is known. A favourable property of the surface gradients estimated by photoclinometry is that they are not affected by regularisation conditions such as smoothness of the surface. On the other hand, spurious artifacts tend to occur perpendicular to the direction of incident light.

However, such assumptions are obsolete in the case of independent depth information available on large spatial scales. Hence, instead of setting the reflectance error E_R to zero independently for each pixel, we minimise a weighted sum of the reflectance error E_R according to Eq. (21.3) and the DEM error E_{DEM} according to Eq. (21.5). Therefore, in analogy to classical photoclinometry, our extended photoclinometry scheme does not take into account a regularisation term such as smoothness or integrability of the surface gradients. Rather, we perform an independent pixel-wise minimisation of E_{Σ} according to Eq. (21.6) with $\gamma = 0$ [11]. In order to examine the behaviour of this minimisation, the Hessian matrix of E_{DEM} is required. For its first diagonal element we obtain the expression

$$\begin{aligned} \frac{\partial^2 E_{DEM}}{\partial p^2} = & \sum_{i=-K/2}^{K/2} \sum_{j=-L/2}^{L/2} F_{\sigma_{DEM}}(-i, -j) A(u+i, v+j) \left[\sum_{k=-K/2}^{K/2} \sum_{l=-L/2}^{L/2} F_{\sigma_{DEM}}(k, l) \right. \\ & \times \left. \frac{\partial}{\partial p} \left(- \frac{\partial z_{DEM}}{\partial x} \Big|_{u+k+i, v+l+j} + p(u+k+i, v+l+j) \right) \right] \end{aligned}$$

$$\begin{aligned}
&= \sum_{i=-K/2}^{K/2} \sum_{j=-L/2}^{L/2} F_{\sigma_{\text{DEM}}}(-i, -j) A(u + i, v + j) \left[\sum_{k=-K/2}^{K/2} \sum_{l=-L/2}^{L/2} F_{\sigma_{\text{DEM}}}(k, l) \right. \\
&\quad \left. \times \frac{\partial}{\partial p} (p(u + k + i, v + l + j)) \right]. \tag{21.12}
\end{aligned}$$

In Eq. (21.12), $k + i = 0$ and $l + j = 0$ must hold for all non-zero summands, and the equation reduces to

$$\frac{\partial^2 E_{\text{DEM}}}{\partial p^2} = \sum_{i=-K/2}^{K/2} \sum_{j=-L/2}^{L/2} F_{\sigma_{\text{DEM}}}^2(-i, -j) \cdot A(u + i, v + j). \tag{21.13}$$

The second derivative with respect to q has the same value. Since neither Eq. (21.9) depends on q nor Eq. (21.10) depends on p , the mixed derivatives are given by

$$\frac{\partial^2 E_{\text{DEM}}}{\partial p \partial q} = \frac{\partial^2 E_{\text{DEM}}}{\partial q \partial p} = 0. \tag{21.14}$$

Therefore, the Hessian matrix of E_{DEM} reduces to a diagonal matrix. Due to the fact that not all filter coefficients of $F_{\sigma_{\text{DEM}}}$ are zero and the pixel area A is positive by definition, all eigenvalues of the Hessian matrix are positive for all pixels. This implies that E_{DEM} possesses only one global minimum. Assuming a minimisation of E_{DEM} with the soft constraint E_R weighted by $1/\delta$, convergence is thus guaranteed for sufficiently large δ .

The resulting surface gradients p and q may be quite far from being integrable, such that we determine the “nearest” surface z based on the approach introduced in [21]. As an alternative to the LOLA DEM, the resulting surface can be used as an initialisation of the variational optimisation scheme described in Sect. 21.3.2. It will be shown in Sect. 21.4 that this initialisation results in a significantly higher absolute reconstruction accuracy.

The albedo map is computed pixel-wise using the initial surface and is then low-pass filtered as explained in Sect. 21.3.2. Since the method by Horn [21] of estimating the surface z from the gradients p and q does not allow large variations of z on large spatial scales, we apply a pyramidal approach, where both the image and the LOLA DEM are downsampled n_{pyr} times by a factor of 2. Starting from the lowest resolution level, the surface and the albedo map are computed and passed on to the next pyramid level until the full image resolution is reached.

21.4 Results of DEM Construction

For DEM construction, we utilise imagery acquired with the Moon Mineralogy Mapper (M^3) on board the Indian Chandrayaan-1 spacecraft. The M^3 instrument is a hyperspectral pushbroom sensor with (in global mode) 85 pixel-synchronous

spectral channels with 20–40 nm per channel with centre wavelengths between 461 and 2,976 nm, where the image resolution typically corresponds to 140 m per pixel [42] (cf. also Table 21.1). The M³ data archive accessible at <http://m3.jpl.nasa.gov/m3data.html> comprises radiance images for each wavelength channel and provides for each image pixel the selenographic longitude and latitude as well as the incidence angle $\theta_i^{(0)}$, the emission angle $\theta_e^{(0)}$, and the phase angle α , where topography is neglected and a smooth spherical surface is assumed for the given values of $\theta_i^{(0)}$ and $\theta_e^{(0)}$. We compute the reflectance error E_R as the sum of squared channel-wise errors according to Eq. (21.3) for channels 50–60, covering the wavelength range from 1,579 to 1,978 nm. As the lunar surface temperature may reach up to 396 K [50], we do not use channels with centre wavelengths beyond 2,000 nm in order to avoid the resulting thermal radiance component. The DEM error according to Eq. (21.5) is computed based on the gridded DEM derived from LOLA data (<http://pds-geosciences.wustl.edu/missions/lro/lola.htm>), which provides absolute elevation values relative to the mean lunar radius of 1,738 km and is georeferenced to the same coordinate system as the M³ images.

Our first example DEM covers the eastern half of the lunar crater Alphonsus, which shows a distinctly non-uniform surface albedo due to the presence of pyroclastic deposits on the crater floor which consist of dark volcanic ash [9]. Bright highland material appears as high-albedo regions. This crater is well suited for demonstrating the capability of the DEM construction algorithm proposed in Sect. 21.3 to separate radiance variations due to topography from those due to non-uniform albedo. The M³ image of Alphonsus, the corresponding LOLA DEM, the refined DEM and the albedo map are shown in Fig. 21.2. Another lunar region displaying distinct albedo variations is the crater Bullialdus (cf. Fig. 21.3). Our refined DEM reveals the terraced structure of the inner crater walls and a multitude of small craters which are invisible in the LOLA DEM. Similarly, we found that despite the high nominal lateral resolution of the GLD100 according to [44], our constructed DEMs reveal much finer details than the GLD100 (cf. also [12]).

No topographic map of sufficiently high lateral resolution is available for the examined regions as ground truth. In order to nevertheless obtain an estimate of the absolute accuracy, a synthetic image of Bullialdus crater was created by illuminating the constructed DEM using the inferred albedo map. The illumination and viewing direction were adopted from the original M³ image. This synthetic image was used as an input image for our DEM construction algorithm. When the variational optimisation scheme is initialised with the LOLA DEM, the reconstruction error (RMSE) corresponds to 54 m, while it becomes as low as 9 m when the result of the extended photoclinometry scheme is used for initialisation. The RMSE of the inferred albedo map at 1,978 nm wavelength amounts to 0.007 and 0.005, corresponding to 1.8 and 1.3 % of the mean albedo of 0.391, respectively.

These results were obtained by performing 8 iterations of the variational approach (cf. Sect. 21.3.2) with σ_w decreasing from 11 to 7 pixels, $\sigma_{\text{DEM}} = 7$ pixels, $\gamma = 9 \times 10^{-4}$, and $\delta = 2.5 \times 10^{-5}$. The values of γ and δ have been chosen as small as possible for the optimisation scheme to converge in order to maximise

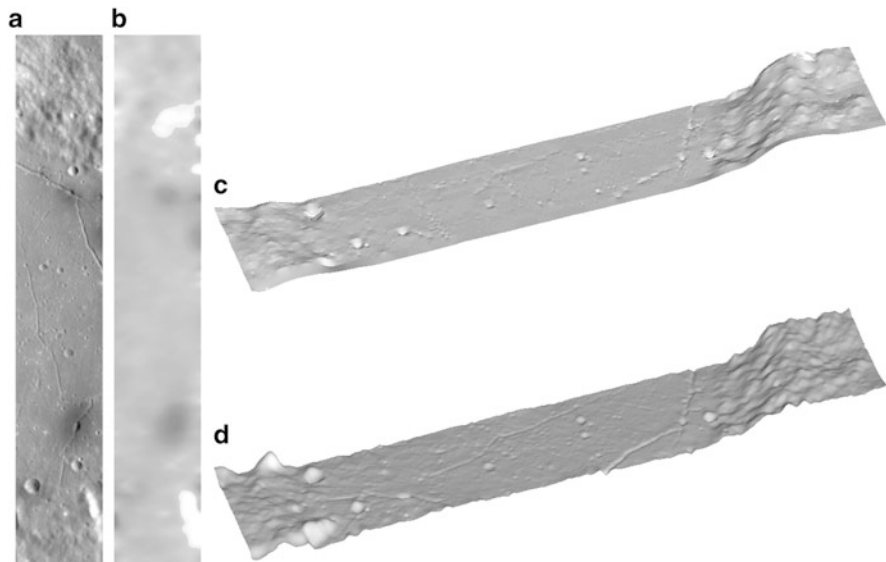


Fig. 21.2 Part of the floor of the lunar crater Alphonsus. **(a)** M^3 radiance image at 1,978 nm (Courtesy NASA/JPL-Caltech). **(b)** Map of the single-scattering albedo w at 1,978 nm, obtained with $\sigma_w = 5$ pixels. The grey value range is 0–0.6. **(c)** LOLA DEM. **(d)** Refined DEM. In the shaded perspectival views of the DEMs, the vertical axis is three times exaggerated and the albedo is assumed to be constant

the influence of the reflectance error E_R . The variational optimisation scheme was initialised by the result of the extended photoclinometry method outlined in Sect. 21.3.3, where we have set $\sigma_w = 16$ pixels due to the low effective lateral resolution of the LOLA DEM, $\delta = 0.05$, and $n_{\text{pyr}} = 4$. Furthermore, we achieved a favourable convergence behaviour when applying the pyramidal approach also in the variational optimisation. As the photoclinometry result used for initialisation is already close to the final result, we set $n_{\text{pyr}} = 1$ in the variational scheme.

21.5 Calibration of Hyperspectral Imagery

This section describes the preprocessing and normalisation of the hyperspectral image data used for DEM construction. Furthermore, the topography dependence of the spectral parameters extracted from the pixel spectra is regarded, and an empirical topography correction scheme based on a principal component analysis (PCA) is proposed. The topography dependence of spectral ratios extracted from Clementine multispectral imagery and the correspondingly estimated abundances of chemical compounds in the lunar soil is shown in [24]. As our method is based on the ratios of spectra acquired at almost identical phase angles α (the variation of α within an

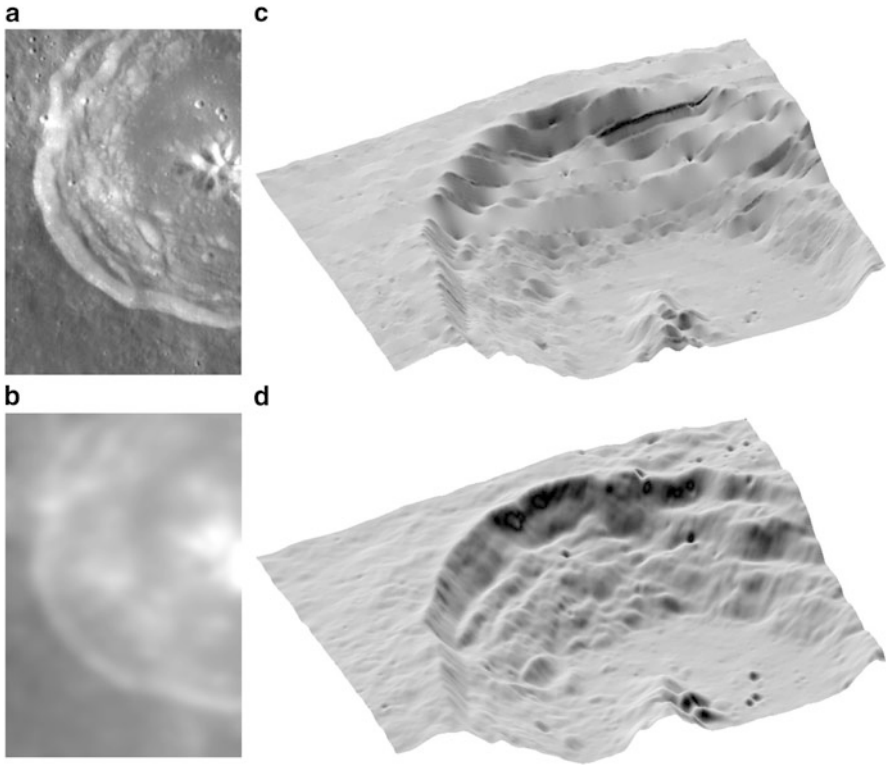


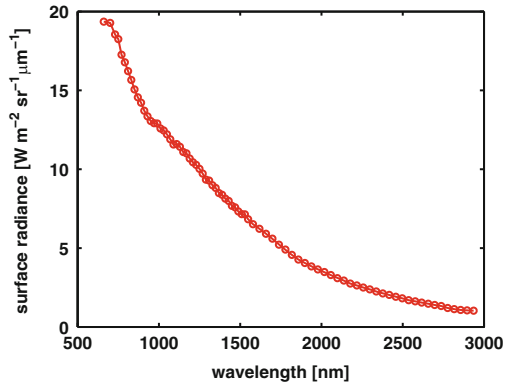
Fig. 21.3 Lunar crater Bullialdus. **(a)** M^3 radiance image at 750 nm (Courtesy NASA/JPL-Caltech). **(b)** Map of the single-scattering albedo w at 750 nm, obtained with $\sigma_w = 9$ pixels. The grey value range is 0–0.35. **(c)** LOLA DEM. **(d)** Refined DEM. In the shaded perspectival views of the DEMs, the vertical axis is three times exaggerated and the albedo is assumed to be constant

image is always smaller than a few degrees), the approach based on an empirical phase angle dependent photometric function suggested in [19] for M^3 data is not able to perform such a correction of the spectra with respect to local topography.

21.5.1 *Preprocessing and Normalisation of Reflectance Spectra*

In our spectral analyses we omit M^3 channels 1–5 (which are known to be poorly calibrated [23]) and 85 (this channel is also omitted in [19]) and only use channels 6–84, covering the wavelength range from 661 to 2,936 nm (cf. Fig. 21.4 for a typical observed radiance spectrum). In remote sensing, it is a standard procedure to take into account the thermal emission component of the observed spectra [45].

Fig. 21.4 Typical M³ radiance spectrum (channels 6–84 covering the wavelength range 661–2,936 nm)



At this point, we make the assumption that the observed radiance spectrum L_{λ}^{obs} between about 2,400 and 3,000 nm used for temperature estimation can be modelled as the sum of a reference spectrum and the emission spectrum $\beta B_{\lambda}(T)$ of a black body of temperature T and emissivity β [45], which we assume to be wavelength-independent. Our reference spectrum R_{λ}^{62231} is the extrapolation of a linear fit to the laboratory reflectance spectrum of returned lunar sample no. 62231 (<http://www.planetary.brown.edu/pds/AP62231.html>). The linear fit is performed in the wavelength range 2,400–2,600 nm of the laboratory spectrum and yields the linear reference spectrum

$$R_{\lambda}^{62231} = 0.081151 \lambda[\mu\text{m}] + 0.1423. \quad (21.15)$$

The corresponding radiance spectrum is readily obtained by multiplying R_{λ}^{62231} with the solar irradiance spectrum E_{λ}^{sun} . Hence, the model equation

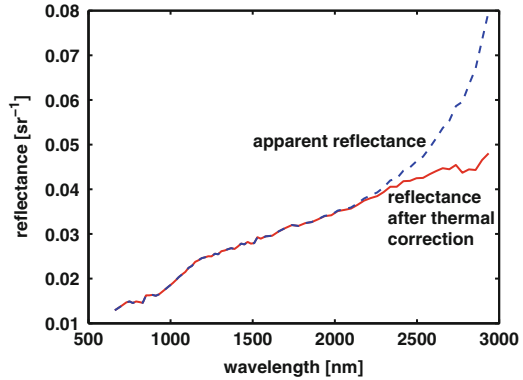
$$L_{\lambda}^{\text{model}} = a R_{\lambda}^{62231} E_{\lambda}^{\text{sun}} + \beta B_{\lambda}(T) \quad (21.16)$$

is fitted to the observed radiance spectrum L_{λ}^{obs} of each M³ pixel in the wavelength range 2,377–2,936 nm, where a is a mean surface reflectivity parameter. This procedure yields maps of the parameters a , β , and T . We always obtained values of the emissivity β close to 1. Notably, due to the limited wavelength coverage of the M³ spectra, it is not possible to reliably estimate temperature values below about 300 K. Finally, the thermally corrected radiance spectrum $L_{\lambda}^{\text{corr}}$ is obtained according to

$$L_{\lambda}^{\text{corr}} = L_{\lambda}^{\text{obs}} - \beta B_{\lambda}(T). \quad (21.17)$$

Figure 21.5 shows a comparison between the apparent reflectance $L_{\lambda}^{\text{obs}}/E_{\lambda}^{\text{sun}}$ obtained without thermal correction and the thermally corrected reflectance $L_{\lambda}^{\text{corr}}/E_{\lambda}^{\text{sun}}$ for an inferred surface temperature of $T = 368$ K. The deviation rapidly increases for wavelengths beyond 2,200 nm.

Fig. 21.5 Comparison between apparent and thermally corrected reflectance for an inferred surface temperature of $T = 368$ K



At this point, we compute for each pixel the true incidence angle θ_i and emission angle θ_e based on the constructed DEM and the angles $\theta_i^{(0)}$ and $\theta_e^{(0)}$ provided with the M^3 image data under the assumption of a smooth spherical surface. The single-scattering albedo $w(x, y)$ obtained based on Eq. (21.11) during the DEM construction process is then inserted into the utilised reflectance model (Hapke IMSA [14–16] or AMSA [17]), using the standard illumination and viewing configuration with $\theta_i^{\text{ref}} = 30^\circ$, $\theta_e^{\text{ref}} = 0^\circ$, and $\alpha^{\text{ref}} = 30^\circ$, which yields the normalised reflectance R_λ^{norm} according to

$$R_\lambda^{\text{norm}}(x, y) = R_{\text{IMSA/AMSA}}(\mu_0^{\text{ref}}, \mu^{\text{ref}}, \alpha^{\text{ref}}, w(x, y)) \quad (21.18)$$

with $\mu_0^{\text{ref}} = \cos(\theta_i^{\text{ref}})$ and $\mu^{\text{ref}} = \cos(\theta_e^{\text{ref}})$. The other parameters of the Hapke model are chosen according to [51] (Moon solution 1 therein).

In this study we use the Hapke IMSA [14–16] and AMSA [17] models for reflectance normalisation. However, the lunar-Lambert model according to Eq. (21.2) is commonly used instead of the Hapke model as the basis for the normalisation of reflectance data [39]. Since this results in a multiplication of the original reflectances by a wavelength-independent factor, wavelength-dependent effects then have to be taken into account by additional correction functions with empirically determined parameters (cf. e.g. [19, 39]).

In the normalised reflectance spectra, one would expect topography effects to be absent. We will see in Sect. 21.5.3, however, that even after normalisation to standard illumination and viewing geometry subtle topography effects can still be observed which may have a significant influence on the extracted spectral parameters.

21.5.2 Extraction of Spectral Parameters

A typical thermally corrected lunar reflectance spectrum is shown in Fig. 21.6. The reflectance strongly increases from visible towards near-infrared wavelengths. The absorption trough around 1,000 nm is due to minerals containing iron in the form of

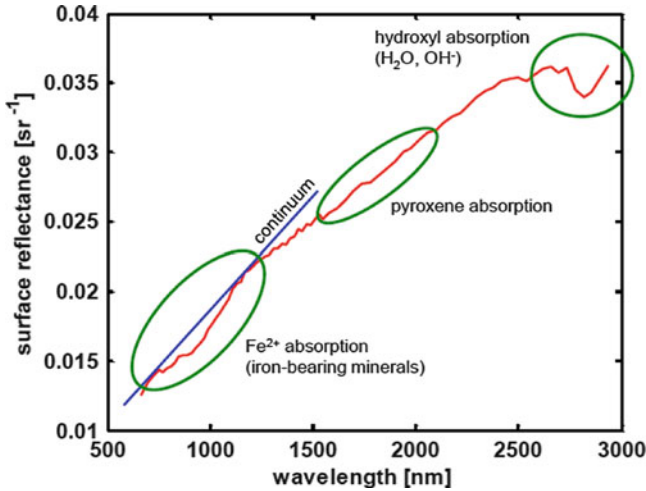


Fig. 21.6 Typical thermally corrected lunar reflectance spectrum, illustrating the primary absorption troughs

Fe^{2+} ions [3,35,48]. A second absorption trough around 2,000 nm can be attributed to the mineral pyroxene [3]. The absorption trough around 2,800 nm is described e.g. in [6], where it is attributed to the presence of water molecules and OH^- ions in the lunar soil. According to [37], they originate from chemical reactions of oxygen contained in the minerals of the lunar surface with protons of the solar wind.

Easily obtainable quantities to characterise the depths of the ferrous absorption trough around 1,000 nm and the hydrous absorption trough around 2,800 nm are the diagnostic spectral ratios $R_{950}^{\text{norm}}/R_{750}^{\text{norm}}$ (cf. e.g. [9]) and $R_{2817}^{\text{norm}}/R_{2657}^{\text{norm}}$, respectively. Additionally, the detailed composition of lunar iron-bearing minerals causes subtle variations of the shape of the ferrous absorption trough, which can be examined based on the continuum-removed spectrum [35,48].

To compute the continuum-removed reflectance spectrum, the normalised reflectance spectrum is smoothed by adapting a curve for which the mean squared deviation from the measured reflectance values and the mean squared second derivative are minimised simultaneously [34]. The spectral continuum is then approximated by a straight line between the smoothed reflectances at 701 and 1,249 nm (cf. [30]). Division of the smoothed reflectance spectrum by the linear continuum then yields the continuum-removed reflectance spectrum [30], to which an interpolation based on the Akima method [2] is applied (cf. Fig. 21.7).

The extracted spectral parameters of the absorption trough around 1,000 nm are (as illustrated in Fig. 21.7) the absorption wavelength λ_{abs} , the full width at half maximum (FWHM), the absorption depth δ (cf. [30]), and the integrated band depth (IBD) [8], corresponding to the area under the trough in Fig. 21.7. The absorption wavelength e.g. allows to differentiate between pyroxenes containing high and low abundances of calcium [35,48]. The absorption depth depends on the amount of

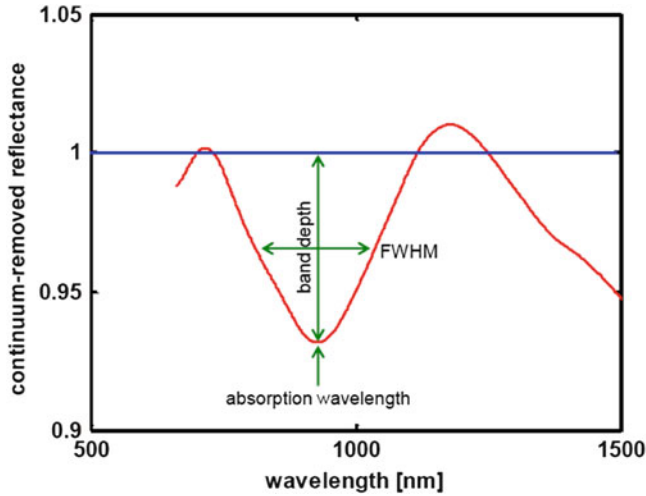


Fig. 21.7 Typical smoothed and continuum-removed reflectance spectrum showing the ferrous absorption trough around 1,000 nm

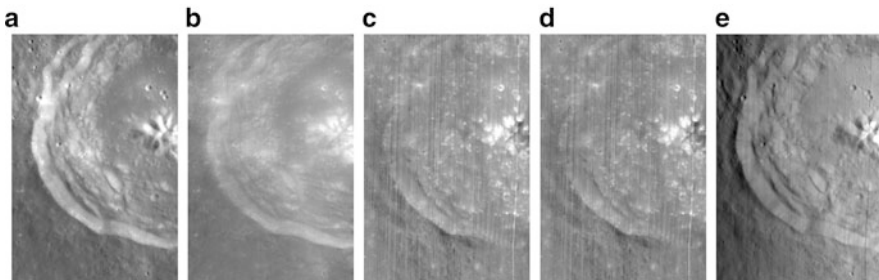


Fig. 21.8 (a) M^3 750 nm radiance image of the crater Bullialdus (Courtesy NASA/JPL-Caltech). (b) Single-scattering albedo w at 750 nm. (c) and (d) Integrated band depth (IBD) of the ferrous absorption trough around 1,000 nm inferred based on the lunar-Lambert and on the Hapke AMSA reflectance function, respectively (grey value range 0–50). (e) Relative difference of the IBD values (grey value range 0–0.15)

mafic minerals [48] and also on the so-called “optical maturity” of the soil [41], i.e. the period of time the surface has been exposed to high-energy solar radiation. A broad absorption, i.e. a large FWHM value, indicates that olivine occurs in the soil [35, 48]. The IBD of the ferrous absorption trough is correlated with the abundance of pyroxene [8].

Figure 21.8 illustrates the difference between the values of the IBD of the ferrous absorption trough inferred based on the wavelength-independent lunar-Lambert reflectance function [38] according to Eq. (21.2) and on the Hapke AMSA reflectance function [17] according to Eq. (21.1), respectively.

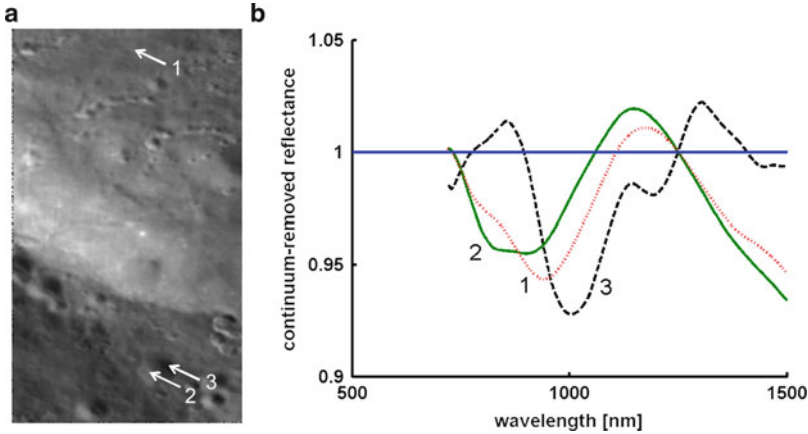


Fig. 21.9 (a) M^3 750 nm radiance image of the Huggins test region (Courtesy NASA/JPL-Caltech). A location on the flat floor of the crater Huggins and two locations inside a small crater just south of Huggins are indicated by arrows. (b) Continuum-removed spectra of the indicated locations. Although from a geological point of view, spectra 2 and 3 from the inner wall of the small crater should be identical, a strong dependence on surface orientation is apparent

21.5.3 Topography Dependence of Spectral Parameters

Figure 21.9 shows continuum-removed spectra of a location on the flat floor of the crater Huggins and two locations inside a small crater just south of Huggins. Although from a geological point of view, spectra 2 and 3 from the inner wall of the small crater should be identical, the spectra appear to be distorted and a strong dependence on surface orientation is visible. In contrast, the spectrum 1 of the flat crater floor displays a regular, symmetric absorption trough. Similar effects are observed for all regions examined in this study. They may in part result from radiance calibration errors e.g. due to a nonlinear behaviour of some M^3 channels. However, one would expect such nonlinearities to result in a radiance dependence of the distortions, whereas in Fig. 21.9 the average radiances of locations 1 and 2 are nearly identical while spectrum 2 displays a distortion but spectrum 1 does not. Hence, inaccuracies of the reflectance model probably also contribute to the topographic effects.

Regarding the spectral parameters, the absorption wavelength λ_{abs} shows the strongest dependence on topography. For a part of the floor of the crater Purbach, Fig. 21.10a, b shows that the slopes inclined towards the sun have much lower absorption wavelengths λ_{abs} than the slopes inclined away from the sun. This systematic effect may lead to geologic misinterpretations as it is very unlikely that e.g. the western and the eastern flank of the mountain range in the image centre consist of strongly different materials, as it would appear from a naive interpretation of the λ_{abs} values.

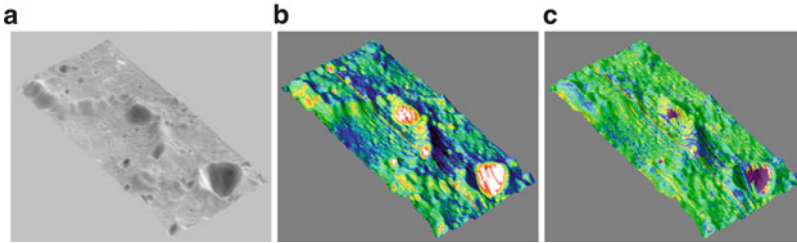


Fig. 21.10 (a) DEM of the floor of the crater Purbach with M³ 750 nm radiance image as overlay (Radiance image: courtesy NASA/JPL-Caltech). (b) Topography dependence of the absorption wavelength λ_{abs} of the ferrous absorption trough. (c) Result of the correction of the topography dependence of λ_{abs} according to Sect. 21.5.4. Low-radiance pixels are masked out in *dark purple* colour. The range of the colour-coded spectral parameter maps is 880–1,000 nm

21.5.4 Empirical Topography Correction

This section describes an empirical approach to the correction of the effect of topography on the M³ spectra. The basic assumption, which is geologically reasonable, is that all pixels on the inclined inner wall of a small crater should have identical reflectance spectra, while inclined and even surface parts may possibly display systematically different spectra.

Hence, the inclined inner wall of a small crater in the region under study is used as a reference region, where the reference spectrum $S_\lambda = \langle R_\lambda \rangle_{\text{ref}}$ is taken to be the average of all spectra of the reference region. For each pixel position (x, y) , the normalised ratio spectrum is then defined as

$$Q_\lambda(x, y) = \frac{R_\lambda(x, y)/S_\lambda}{\langle R_\lambda(x, y)/S_\lambda \rangle_\lambda}. \quad (21.19)$$

A principal component analysis (PCA) of all normalised ratio spectra of the reference region yields a set of PCA components $P_\lambda^{(i)}$ and, for each pixel, a set of PCA coefficients a_i . The DEM constructed according to Sect. 21.3 allows to compute a pixel-wise unit normal vector \mathbf{n} , which in turn yields the surface inclination angle $\sigma = \arccos(n_z)$ and the azimuth angle $\psi = \text{atan2}(n_y, n_x) =: \arctan(n_y/n_x)$, where $\sigma \in [0^\circ, \dots, 90^\circ]$ and $\psi \in [0^\circ, \dots, 360^\circ]$. A polynomial function of second order in σ and eighth order in ψ is fitted to the PCA coefficients extracted from the reference region. For a pixel located at (x, y) outside the reference region, the PCA coefficients $a_i(\sigma(x, y), \psi(x, y))$ are then computed according to the DEM, which yields a corrected normalised ratio spectrum

$$Q_\lambda^{\text{corr}}(x, y) = \frac{R_\lambda}{S_\lambda} - \sum_{i=1}^K a_i(\sigma(x, y), \psi(x, y)) P_\lambda^{(i)} \quad (21.20)$$

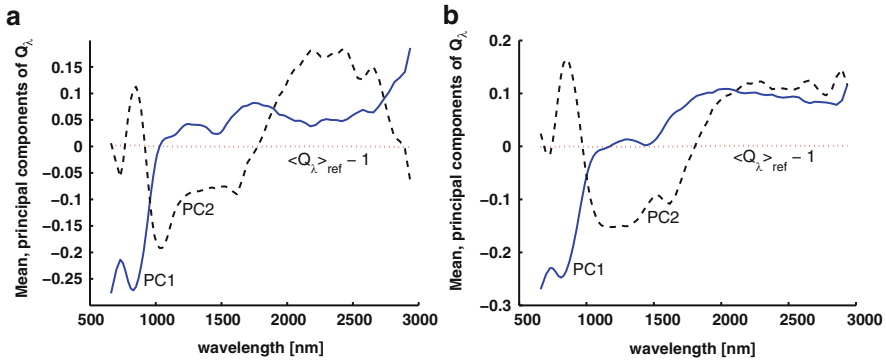


Fig. 21.11 Average value of $Q_\lambda(x, y)$ according to Eq.(21.19) and the first two principal components (denoted by PC1 and PC2), extracted from the pixels belonging (a) to the inner walls of two small craters just south of Huggins and (b) to those of the small crater Purbach A, respectively

and a corrected reflectance spectrum

$$R_\lambda^{\text{corr}}(x, y) = Q_\lambda^{\text{corr}}(x, y) S_\lambda. \quad (21.21)$$

For our two test regions, the first four principal components comprise 98 % of the information, such that we always set $K = 4$ in Eq.(21.20). The average value of $Q_\lambda(x, y)$ is shown along with the first two PCA components for the Huggins and Purbach test regions in Fig. 21.11. The differences between the test regions are due to the higher southern selenographic latitude of the Huggins region, resulting in a more oblique solar illumination angle.

Based on the corrected reflectances, a refined DEM is constructed according to Sect. 21.3.2, where the Hapke IMSA reflectance model is used due to convergence problems with the AMSA model. Finally, the reflectance normalisation and PCA-based topography correction is repeated using the Hapke AMSA model, where it is favourable to neglect low-radiance pixels (e.g. shaded crater walls or mountain flanks) in the analysis due to their very low signal-to-noise ratio.

21.6 Results of Topography Correction and Final DEM Construction

The final DEMs of the Huggins and Purbach test regions are shown in Fig. 21.12, showing a high amount of small-scale surface detail. The spectral parameters extracted from the uncorrected and the final corrected reflectance spectra of these regions are shown in Figs. 21.13 and 21.14, respectively, where dark pixels with 750 nm radiances below $7 \text{ W m}^{-2} \mu\text{m}^{-1} \text{ sr}^{-1}$ are masked out. Figure 21.10c shows

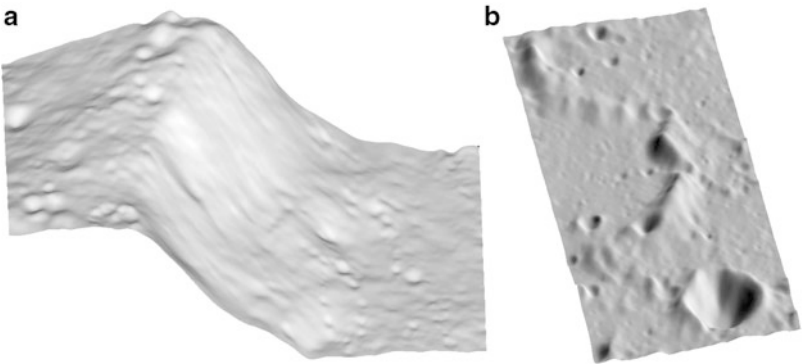


Fig. 21.12 Final DEMs of the test regions (a) Huggins and (b) Purbach. The vertical axis is three times exaggerated. The shaded DEM rather than the original image is used as an overlay, such that all visible small-scale detail is actually present in the DEM and not only in the original image

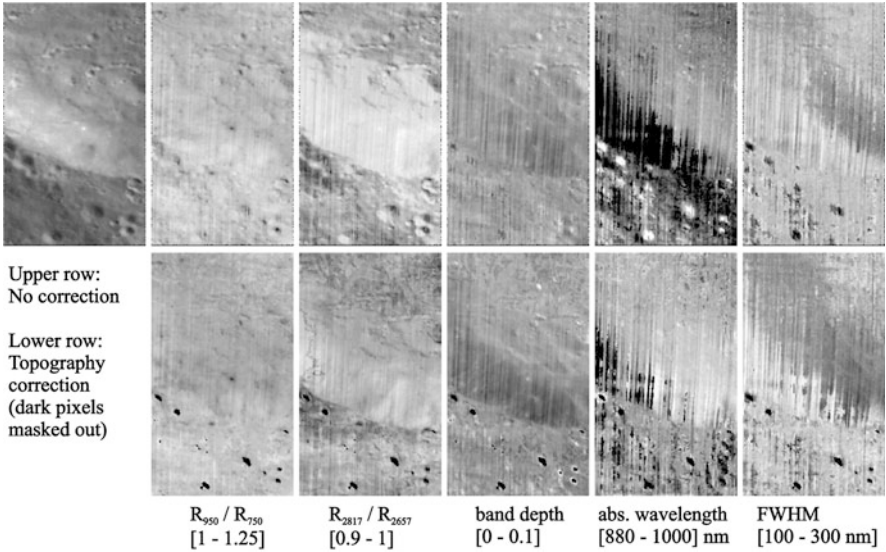


Fig. 21.13 M^3 750 nm radiance image of the Huggins test region (Courtesy NASA/JPL-Caltech) (upper left) and spectral parameters extracted from the uncorrected and from the final corrected reflectance spectra (low-radiance pixels are masked out in black)

the final DEM of the Purbach test region with false-colour overlay of the absorption wavelength λ_{abs} extracted from the uncorrected and final corrected reflectance spectra, respectively. For all examined spectral parameters, the PCA-based correction according to Sect. 21.5.4 is able to eliminate most topographic effects.

As an independent test example, we examine the crater Bullialdus. This crater is located at approximately the same selenographic latitude as the Purbach test region,

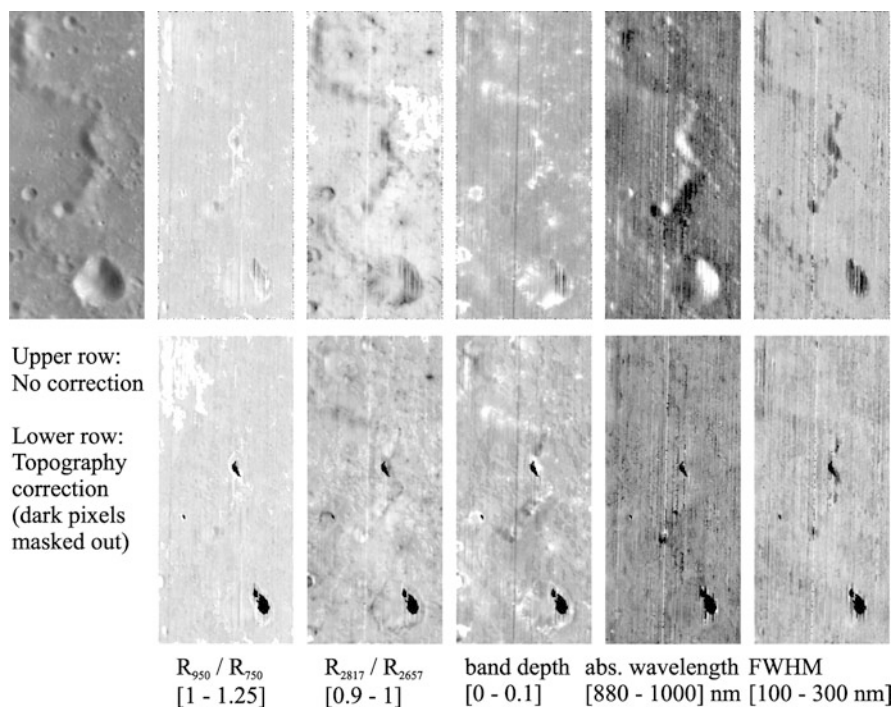


Fig. 21.14 M^3 750 nm radiance image of the Purbach test region (Courtesy NASA/JPL-Caltech) (*upper left*) and spectral parameters extracted from the uncorrected and from the final corrected reflectance spectra (low-radiance pixels are masked out in *black*)

resulting in similar illumination conditions in the corresponding M^3 data. Hence, we use the PCA components $P_{\lambda}^{(i)}$ and the coefficient functions $a_i(\sigma, \psi)$ inferred from the Purbach region in order to compute corrected reflectances according to Eq. (21.21) and extract the corresponding corrected spectral parameters. The spectral parameters extracted from the uncorrected and corrected reflectances are shown in Fig. 21.15 (cf. Fig. 21.3 for the final DEM). Again, the topography correction is most obvious in the map of the absorption wavelength λ_{abs} , which is used as an overlay of the final DEM of Bullialdus in Fig. 21.16. After correction, the crater walls, most of the crater floor, and the even surface outside the crater display similar values of λ_{abs} , only the central peaks still display excessively low absorption wavelengths. These low λ_{abs} values are much more clearly confined to the central peaks than without correction. In [49], the spectral characteristics of the central peaks of Bullialdus are attributed to the occurrence of the mineral norite.

Figure 21.15 shows that the cold, shaded flanks of the central peak of Bullialdus display a stronger hydroxyl absorption (i.e. lower R_{2817}/R_{2657} ratio) than the warmer crater floor. This effect is not eliminated by the empirical correction approach. Temperatures below 250–300 K cannot be estimated reliably due to the

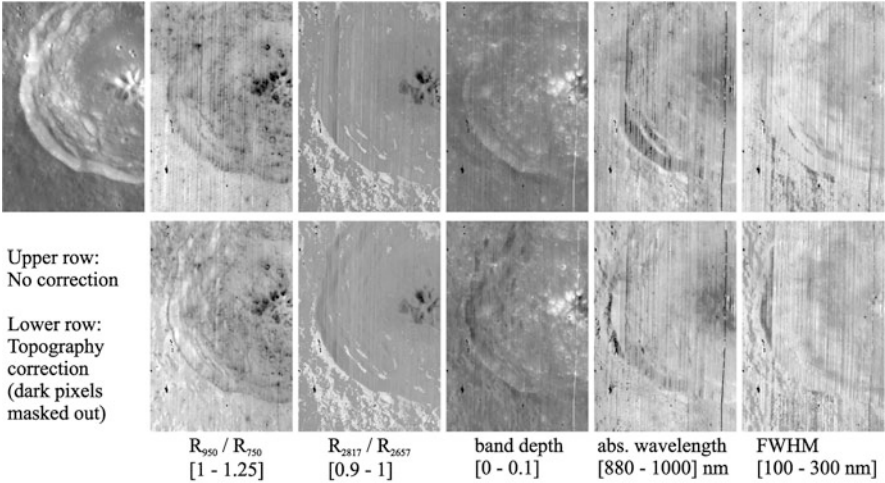


Fig. 21.15 M^3 750 nm radiance image of Bullialdus crater (Courtesy NASA/JPL-Caltech) (*upper left*) and spectral parameters extracted from the uncorrected and from the final corrected reflectance spectra

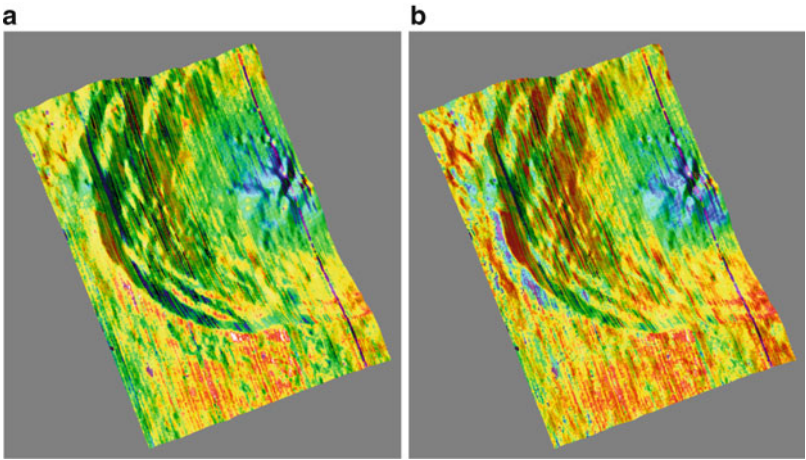


Fig. 21.16 Final DEM of Bullialdus crater with false-colour overlay of the absorption wavelength λ_{abs} (range: 880–1,000 nm) extracted (a) from the uncorrected and (b) from the final corrected reflectance spectra, respectively

limited spectral range, such that for these pixels no thermal correction can be performed. The high R_{2817}/R_{2657} values southwest of the crater appear to be due to cool surface parts with temperatures just below the detection threshold, for which the thermal correction is inaccurate. Generally spoken, it is not possible based on the available data to distinguish topography effects on the R_{2817}/R_{2657} ratio (cf. also Figs. 21.13 and 21.14) from thermal effects.

21.7 Summary and Conclusion

A method for the construction of lunar DEMs which combines surface gradients obtained by photoclinometry and shape from shading with absolute depth data (here: lunar orbital LIDAR data) by exploiting their respective advantages has been presented. The lunar surface has a non-Lambertian reflectance behaviour and a non-uniform albedo. In a first step, the surface gradients are estimated based on an extended photoclinometry approach which takes into account both image and LIDAR data, and the surface is reconstructed by integration. The second step consists of the minimisation of a global error functional based on a variational approach in order to combine the surface gradient information on small spatial scales and the LIDAR data on large spatial scales, where the result of the first step is used for initialisation. This framework has been applied to the construction of DEMs of lunar surface regions. Based on the available hyperspectral imagery, the obtained DEMs have been used to normalise the wavelength-dependent surface reflectance to a standard illumination and viewing geometry. In this context, an empirical, PCA-based correction approach has been proposed to compensate the detected systematic topography-dependent distortions of the pixel spectra which affect the extracted spectral parameters. Relying on the corrected surface reflectance data, refined DEMs have been constructed and spectral parameter maps have been obtained in which (except for the hydroxyl absorption) topographic effects are nearly completely removed.

References

1. Agrawal, A., Raskar, R., Chellappa, R.: What is the range of surface reconstructions from a gradient field? In: Leonardis, A., Bischof, H., Pinz, A. (eds.) *Proceedings of European Conference on Computer Vision. Lecture Notes in Computer Science*, vol. 3951, pp. 578–591. Springer (2006)
2. Akima, H.: A new method of interpolation and smooth curve fitting based on local procedures. *J. Assoc. Comput. Mach.* **17**(4), 589–602 (1970)
3. Burns, R.G., Abu-Eid, R.M., Huggins, F.E.: Crystal field spectra of lunar pyroxenes. In: *Proceedings of Lunar Science Conference*, vol. 2, pp. 533–543. Lunar and Planetary Institute, Houston (1972)
4. Bussey, D.B.J., McGovern, J.A., Spudis, P.D., Neish, C.D., Sørensen, S.A.: Lunar polar illumination conditions derived using Kaguya laser data. In: *Proceedings of Annual Meeting of LEAG*. Lunar and Planetary Institute, Houston (2009)
5. Chandrasekhar, S.: *Radiative Transfer*. Dover, New York (1960)
6. Clark R., Pieters, C.M., Green, R.O., Boardman, J., Buratti, B.J., Head, J.W., Isaacson, P.J., Livo, K.E., McCord, T.B., Nettles, J.W., Petro, N.E., Sunshine, J.M., Taylor, L.A.: Water and Hydroxyl on the Moon as seen by the Moon Mineralogy Mapper (M³). In: *Proceedings of Lunar Planetary Science XXXXI*, abstract #2302. Lunar and Planetary Institute, Houston (2010)
7. Cryer, J.E., Tsai, P.-S., Shah, M.: Integration of shape from shading and stereo. *Pattern Recognit.* **28**(7), 1033–1043 (1995)

8. Dhingra, D., Pieters, C.M., Isaacson, P., Staid, M., Mustard, J., Klima, R., Taylor, L.A., Kramer, G., Nettles, J., M³ team: Spectroscopic signature of the high titanium basalts at mare tranquillitatis from Moon Mineralogy Mapper (M³). In: Proceedings of Lunar Planetary Science XXXXI, abstract #2494. Lunar and Planetary Institute, Houston (2010)
9. Gaddis, L.R., Staid, M.I., Tyburczy, J.A., Hawke, B.R., Petro, N.E.: Compositional analyses of lunar pyroclastic deposits. *Icarus* **161**, 262–280 (2003)
10. Grieger, B., Beauvivre, S., Despan, D., Erard, S., Josset, J.-L., Koschny, D.: Investigating a peak of (almost) eternal light close to the lunar south pole with SMART-1/AMIE images. In: Proceedings of European Planetary Science Congress, EPSC2008-A-00205, Münster, Germany (2008)
11. Grumpe, A., Wöhler, C.: DEM construction and calibration of hyperspectral image data using pairs of radiance images. In: Proceedings of IEEE International Symposium on Image and Signal Processing and Analysis, Dubrovnik, Croatia, pp. 609–614 (2011)
12. Grumpe, A., Wöhler, C.: Image-based construction of lunar digital elevation models of very high lateral resolution. In: Proceedings of Lunar Planetary Science XXXXIII, abstract #2597. Lunar and Planetary Institute, Houston (2012)
13. Grumpe, A., Herbort, S., Wöhler, C.: 3D reconstruction of non-Lambertian surfaces with non-uniform reflectance parameters by fusion of photometrically estimated surface normal data with active range scanner data. In: Proceedings of Oldenburger 3D-Tage, Oldenburg, Germany, pp. 54–61 (2011)
14. Hapke, B.W.: Bidirectional reflectance spectroscopy 1: theory. *J. Geophys. Res.* **86**, 3039–3054 (1981)
15. Hapke, B.W.: Bidirectional reflectance spectroscopy 3: correction for macroscopic roughness. *Icarus* **59**, 41–59 (1984)
16. Hapke, B.W.: Bidirectional reflectance spectroscopy 4: the extinction coefficient and the opposition effect. *Icarus* **67**, 264–280 (1986)
17. Hapke, B.W.: Bidirectional reflectance spectroscopy 5: the coherent backscatter opposition effect and anisotropic scattering. *Icarus* **157**, 523–534 (2002)
18. Herbort, S., Grumpe, A., Wöhler, C.: Reconstruction of non-Lambertian surfaces by fusion of shape from shading and active range scanning. In: Proceedings of IEEE International Conferences on Image Processing, Brussels, Belgium, pp. 17–20 (2011)
19. Hicks, M.D., Buratti, B.J., Nettles, J., Staid, M., Sunshine, J., Pieters, C.M., Besse, S., Boardman, J.: A photometric function for analysis of lunar images in the visual and infrared based on Moon Mineralogy Mapper observations. *J. Geophys. Res.* **116**, E00G15 (2011). doi:10.1029/2010JE003733
20. Horn, B.K.P.: Shape from shading: a method for obtaining the shape of a smooth opaque object from one view. MIT Technical Report 232, Massachusetts Institute of Technology (1970)
21. Horn, B.K.P.: Robot Vision. MIT Press, Cambridge, MA (1986)
22. Horn, B.K.P.: Height and gradient from shading. AI Memo 1105A, MIT AI Lab (1989)
23. Isaacson, P.: M³ overview and working with M³ data. M³ Data Tutorial at Lunar Planetary Science XXXXII. <http://m3.jpl.nasa.gov/pubs/Isaacson.M3DataWorkshop.LPSC2011.pdf> (2011)
24. Jolliff, B.L.: Clementine UVVIS multispectral data and the Apollo 17 landing site: what can we tell and how well? *J. Geophys. Res.* **104**(E6), 14123–14148 (1999)
25. Joshi, N., Kriegman, D.J.: Shape from varying illumination and viewpoint. In: Proceedings of the International Conference on Computer Vision. IEEE, New York (2007)
26. Josset, J.-L., et al.: Science objectives and first results from the SMART-1/AMIE multicolour micro-camera. *Adv. Space Res.* **37**, 14–20 (2006)
27. Kieffer, H.H., Stone, T.C.: The spectral irradiance of the Moon. *Astron. J.* **129**, 2887–2901 (2005)
28. Kirk, R.L., Soderblom, L.A., Howington-Kraus, E., Archinal, B.: USGS high-resolution topomapping of Mars with Mars orbiter camera narrow-angle images. In: Proceedings of ISPRS Symposium on Geospatial Theory, Processing and Applications. International Society for Photogrammetry and Remote Sensing (2002)

29. Kozera, R.: Existence and uniqueness in photometric stereo. *Appl. Math. Comput.* **44**(1), 1–103 (1991)
30. Le Mouélic, S., Lucey, P.G., Langevin, Y., Hawke, B.R.: Calculating iron contents of lunar highland materials surrounding Tycho crater from integrated Clementine UV-visible and near-infrared data. *J. Geophys. Res.* **107**(E10), 5074 (2002). doi:10.1029/2000JE001484
31. Li, R., Wang, W., He, S., Yan, L., Meng, X., Crawford, J., Robinson, M.S., Tran, T., Archinal, B.A., the LROC Team: Latest results of 3D topographic mapping using lunar reconnaissance orbiter narrow-angle camera data. In: *Proceedings of Lunar Planetary Science XXXII*, abstract #2010. Lunar and Planetary Institute, Houston (2011)
32. Lim, J., Ho, J., Yang, M.-H., Kriegman, D.: Passive photometric stereo from motion. In: *Proceedings of International Conference on Computer Vision*, vol. 2, pp. 1635–1642. IEEE, New York (2005)
33. Lohse, V., Heipke, C., Kirk, R.L.: Derivation of planetary topography using multi-image shape-from-shading. *Planet. Space Sci.* **54**, 661–674 (2006)
34. Marsland, S.: *Machine Learning: An Algorithmic Perspective*. Chapman & Hall/CRC Machine Learning and Pattern Recognition Series. CRC, Boca Raton (2009)
35. Matsunaga, T., et al.: Discoveries on the lithology of lunar crater central peaks by SELENE Spectral Profiler. *Geophys. Res. Lett.* **35**, L23201 (2008). doi:10.1029/2008GL035868
36. Mattson, S., Ojha, A., Ortiz, A., McEwen, A.S., Burns, K.: Regional digital terrain model production with LROC-NAC. In: *Proceedings Lunar Planetary Science XXXIII*, abstract #2630. Lunar and Planetary Institute, Houston (2012)
37. McCord, T.B., Taylor, L.A., Orlando, T.M., Pieters, C.M., Combe, J.-Ph., Kramer, G., Sunshine, J.M., Head, J.W., Mustard, J.F.: Origin of OH/Water on the lunar surface detected by the Moon Mineralogy Mapper. In: *Proceedings of Lunar Planetary Science XXXI*, abstract #1860. Lunar and Planetary Institute, Houston (2010)
38. McEwen, A.S.: Photometric functions for photoclinometry and other applications. *Icarus* **92**, 298–311 (1991)
39. McEwen, A.S., Eliason, E., Lucey, P., Malaret, E., Pieters, C., Robinson, M., Sucharski, T.: Summary of radiometric calibration and photometric normalization steps for the Clementine UVVIS images. In: *Proceedings Lunar Planetary Science XXIX*, abstract #1466. Lunar and Planetary Institute, Houston (1998)
40. Nehab, D., Rusinkiewicz, S., Davis, J., Ramamoorthi, R.: Efficiently combining positions and normals for precise 3D geometry. *ACM Trans. Graph. (Proc. SIGGRAPH)* **24**(3), 536–543 (2005)
41. Nettles, J.W., Besse, S., Boardman, J., Combe, J.-P., Clark, R., Dhingra, D., Isaacson, P., Klima, R., Kramer, G., Petro, N.E., Pieters, C.M., Staid, M., Taylor, L.A.: Progress toward a new lunar optical maturity measure based on Moon Mineralogy Mapper (M^3) data. In: *Proceedings of Lunar Planetary Science XXXI*, abstract #2217. Lunar and Planetary Institute, Houston (2010)
42. Pieters, C.M., et al.: The Moon Mineralogy Mapper (M^3) on Chandrayaan-1. *Curr. Sci.* **96**(4), 500–505 (2009)
43. Robinson, M.S., et al.: Lunar reconnaissance orbiter camera (LROC) instrument overview. *Space Sci. Rev.* **150**, 81–124 (2010)
44. Scholten, F., Oberst, J., Matz, K.-D., Roatsch, T., Wählisch, M., Robinson, M.S., the LROC Team: GLD100 – the global lunar 100 meter raster DTM from LROC WAC Stereo models. In: *Proceedings of Lunar Planetary Science XXXII*, abstract #2046. Lunar and Planetary Institute, Houston (2011)
45. Schowengerdt, R.A.: *Remote Sensing: Models and Methods for Image Processing*. Academic Press, Burlington (2006)
46. Simakov, D., Frolova, D., Basri, R.: Dense shape reconstruction of a moving object under arbitrary, unknown lighting. In: *Proceedings of International Conferences on Computer Vision*, vol. 2, pp. 1202–1209. IEEE, New York (2003)
47. Simchony, T., Chellappa, R., Shao, M.: Direct analytical methods for solving poisson equations in computer vision problems. *IEEE Trans. Pattern Anal. Mach. Intell.* **12**(5), 435–446 (1990)

48. Smrekar, S., Pieters, C.M.: Near-infrared spectroscopy of probable impact melt from three large lunar highland craters. *Icarus* **63**, 442–452 (1985)
49. Tompkins, S., Pieters, C.M., Mustard, J.F., Pinet, P., Chevrel, S.D.: Distribution of materials excavated by the lunar crater Bullialdus and implications for the geologic history of the Nubium region. *Icarus* **110**(2), 261–274 (1994)
50. Vaniman, D., Reedy, R., Heiken, G., Olhoeft, G., Mendell, W.: The lunar environment. In: Heiken, G., Vaniman, D., French, B.M. (eds.) *Lunar Sourcebook*. Cambridge University Press, Cambridge, UK (1991)
51. Warell, J.: Properties of the Hermean regolith: IV. Photometric parameters of Mercury and the Moon contrasted with Hapke modelling. *Icarus* **167**(2), 271–286 (2004)
52. Wilhelms, D.E.: A photometric technique for measurement of lunar slopes. In: *Astrogeologic Studies, Annual Progress Report, Part D: Studies for Space Flight Program*, USGS preliminary report, United States Geological Survey, pp. 1–12 (1964)
53. Wöhler, C., d’Angelo, P.: Stereo image analysis of non-Lambertian surfaces. *Int. J. Comput. Vis.* **81**(2), 172–190 (2009)
54. Woodham, R.J.: Photometric method for determining surface orientation from multiple images. *Opt. Eng.* **19**(1), 139–144 (1980)
55. Zhang, L., Curless, B., Hertzmann, A., Seitz, S.M.: Shape and motion under varying illumination: unifying structure from motion, photometric stereo, and multi-view stereo. In: *Proceedings of International Conference on Computer Vision*, vol. 1, pp. 618–626. IEEE, New York (2003)